Check for updates

Electrochemical properties of PX-phase PbTiO₃ electrode for sodium ion batteries†

Yixiang Zhang,[a] Muwei Ji,[abc] Ziyi Liu,[a] Yiqing He,[a] Yao Hu,[a] Qinghua Yang,[a] Bo Li[a] and Jin Wang [ID] *[a]

PX-phase PbTiO₃ (PT) nanowires have been investigated for the first time as an anode material for sodium ion batteries (NIBs). Their sodium storage properties are presented by employing sodium-carboxyl-methyl-cellulose (CMC) and styrene-butadiene-rubber (SBR) as binders. Electrochemical results show that the PT/CMC–SBR electrode delivers a specific capacity of 84.2 mA h g⁻¹ after 100 cycles. The PT nanowires are found to undergo an irreversible conversion reaction to transform into a composite structure composed of 5–8 nm Pb nanoparticles uniformly dispersed in the amorphous matrixes in the initial discharge process. In the subsequent cycling process, the discharge capacity is primarily attributed to alloying reaction between Pb and Na and conversion reaction between Pb and PbO₂. Furthermore, we use polyvinylidene fluoride (PVDF) instead of CMC–SBR as binder to study the influence of binders on the electrochemical performance of PX-phase PT anode. It is found that PT/CMC–SBR electrode exhibits better electrochemical properties than PT/PVDF electrode in both cyclic performance and rate capability. Detailed analysis is conducted to understand the underlying mechanism for the distinct NIBs anode performance of PT nanowires caused by use of different binders. It is found that compared to PT/CMC–SBR electrode, the conversion reaction between Pb and PbO₂ is missing in the PT/PVDF electrode, and that Pb active material has diffused out from the wires and reprecipitated as microsized hexagonal particles during the discharge/charge process, leading to the inferior electrochemical performance of PT/PVDF electrodes. This work signifies the importance of binders to optimize the electrochemical performance for alloy anode materials in NIBs.

Introduction

In recent years, sodium-ion batteries (NIBs) have attracted lots of attention due to the abundance, low cost and environmental friendliness of sodium resources.[1,2] A number of cathode materials are proposed for NIBs, including Na$_x$CoO$_2$,[3] Na$_x$MnO$_2$,[4] NaFeO$_2$,[5] NaV$_6$O$_{15}$,[6] NaFePO$_4$,[7] and Na$_3$V$_2$(PO$_4$)$_3$[8] *et al.* A wide category of candidate materials for NIBs anode materials have also been intensively investigated. It turns out sodium ions could not intercalate into graphite sheets which is the sate-of-the-art lithium-ion anode material.[9] On the contrary, hard carbon,[10] petroleum coke[11] and carbon microspheres[12] show good sodium storage capability. TiO$_2$,[13,14] sodium titanates[15,16] and alloying materials such as Sn,[17] Sb,[18,19] SnSb[20] and SnO$_2$[21,22] are also reported as promising sodium-ion anode materials. However, a key issue for alloying anode materials is significant volume change and agglomeration of nanoparticles during charge/discharge

process, which results in the material pulverization, capacity reduction and unsatisfactory cyclic performance.[23] Therefore, delicate composite systems such as core/shell structures[24] or introducing secondary carbon phases[20] are explored to solve the problem. Another important factor in the stabilization of the cycling capacity of alloying anode is binders, which can maintain the structural integrity during the volume change. Polyvinylidene fluoride (PVDF) is a most conventional binder in NIBs. Recently, alloy anodes with some other kinds of binders such as sodium-carboxyl-methyl-cellulose (CMC), polyacrylic acid (PAA), sodium polyacrylate (PANa), and styrene-butadiene-rubber (SBR) have been reported to exhibit better performance than that with PVDF in NIBs.[25–27]

Sodium has been shown to electrochemically insert into Pb at room temperature. The full sodiation lead of Na$_{15}$Pb$_4$ phase has a capacity of 485 mA h g⁻¹, corresponding to a volume expansion of 365%. Both Jow *et al.*[28] and Komaba *et al.*[29] suggested the formation of NaPb$_3$, NaPb, Na$_5$Pb$_2$ and Na$_{15}$Pb$_4$ in order during the sodiation of lead, but without any evidence of their formation. However, it was demonstrated by Ellis *et al.*[30] that NaPb$_3$, NaPb, Na$_9$Pb$_4$ and Na$_{15}$Pb$_4$ were formed sequentially instead of NaPb$_3$, NaPb, Na$_5$Pb$_2$ and Na$_{15}$Pb$_4$ during the sodiation, when they studied the sodiation process of lead film by *in situ* XRD. Recently, Darwiche *et al.*[31] utilized *in situ* XRD to study the phase

[a]*Advanced Materials Institute, Graduate School at Shenzhen, Tsinghua University, Shenzhen 518055, P. R. China. E-mail: Wang.jin@sz.tsinghua.edu.cn*

[b]*Institute of Chemistry, Chinese Academy of Science, Beijing, 100190, P. R. China*

[c]*College of Chemistry and Environmental Engineering, Shenzhen University, Shenzhen, 518061, P. R. China*

transformation of the bulk lead during sodiation process and reported phase formation process of Na–Pb alloy consistent with that found by Ellis *et al.* In addition, the highly loaded Pb in this system showed sustainable capacity retention of 464 mA h g^{-1} after 50 cycles at 13 mA g^{-1}. Pb(NO$_3$)$_2$ was also investigated as anode materials for sodium ion batteries with a specific capacity of 81.5 mA h g^{-1} after 50 cycles.[32] Different from the case of bulk Pb, the sodiation process of Pb(NO$_3$)$_2$ does not show four distinct potential plateaus.

In our previous studies, it was found that PX-phase PbTiO$_3$ (PT) presents high reversible specific capacity, excellent cycling property and rate capacity in the lithium-ion batteries because it can combine the high specific capacity of Pb and good rate capability of TiO$_2$-based systems. In this work, PX-phase PbTiO$_3$ nanowires are studied as novel anode material for NIBs. Electrochemical results show that the PT/CMC–SBR electrode delivers a specific capacity of 84.2 mA h g^{-1} after 100 cycles. The PT nanowires are found to undergo an irreversible conversion reaction to transform into a composite structure composed of 5–8 nm Pb nanoparticles uniformly dispersed in the amorphous matrixes in the initial discharge process. In the subsequent cycling process, the discharge capacity was primarily attributed to alloying reaction between Pb and Na and conversion reaction between Pb and PbO$_2$. Furthermore, we use PVDF instead of CMC–SBR as binder to study the influence of binders on the electrochemical performance of PX-phase PT anode. It is found that PT/CMC–SBR electrode exhibited better electrochemical properties than PT/PVDF electrode in both cyclic performance and rate capability. Detailed analysis is conducted to understand the underlying mechanism for the distinct NIBs anode performance of PT nanowires caused by use of different binders. This work signifies the importance of binders to optimize the electrochemical performance of alloy anode materials in NIBs.

Experiments

Materials preparation

PX-phase PT nanowires are prepared by a reported hydrothermal method.[33] 4 mmol of Ti(OC$_4$H$_9$)$_4$ (Sigma-Aldrich) is first dissolved in 8 mL of ethanol and the obtained transparent solution is hydrolyzed in 8 mL of deionized H$_2$O. Subsequently, 20 mmol of KOH (Sigma-Aldrich), 5.2 mmol of Pb(NO$_3$)$_2$ (Alfa Aesar), and 0.05 g of polyvinyl alcohol (PVA) (Alfa Aesar) are added and mixed homogeneously under stirring. The volume of the mixture is then adjusted to 40 mL with deionized H$_2$O, and transfered into a 50 mL Teflon-lined autoclave. Hydrothermal treatment is carried out at 200 °C for 3.5 h, followed by washing with deionized H$_2$O until neutral pH is achieved. The Pb oxide remnant is removed with 10 wt% CH$_3$COOH aqueous solution. The final pure PX-phase sample is obtained by another cycle of washing with deionized H$_2$O and dried at 60 °C in air.

Material characterization

X-ray diffraction (XRD) is conducted using a Rint-2000V/PC diffractometer (Rigaku, Japan) with Cu/Kα radiation (λ = 1.5406 Å). The scanning electron microscope (SEM, ZEISS

SUPRA® 55), which is equipped with an EDS detector (Oxford X-Max 20), is used for the morphologies and EDS analysis of materials. Transmission electron microscopy (TEM) analysis is conducted with Tecnai G2 F30. X-ray photoelectron spectroscopy (XPS) is performed using PHI-5000 Versaprobe II (Ulvac-Phi, Japan).

Electrochemical measurements

Electrochemical tests of the anode materials are carried out using coin cell CR2032. For preparing the PT/PVDF electrodes, a slurry of 80% active materials (PX-phase PT), 10% carbon black (Super P) and 10% PVDF in NMP is coated onto a copper foil and then dried at 110 °C over night in a vacuum oven. The procedure for preparing PT/CMC–SBR electrodes is the same except that a mixture of 5 wt% CMC (1.5 wt% aqueous solution) and 5 wt% SBR (50 wt% aqueous solution) is used instead of PVDF. The sodium cells are assembled in an argon-filled glove box (mbraum) with metallic sodium wafer as the counter electrode, glass fibers as the separator, and 1 M NaClO$_4$ in 1 : 1 ethylene carbonate (EC)/dimethylcarbonate (DMC) as the electrolyte. All the cells are aged for 12 h before conducting the electrochemical measurements. The galvanostatic discharge–charge tests are conducted in the voltage window of 0.005–3 V at room temperature using LanHe BT2000 multichannel testing equipment. Cyclic voltammograms (CVs) measurement is conducted using a Bio-Logic VMP2 multichannel potentiostat. The scan rate and potential interval in the CV tests are set at 0.1 mV s^{-1} and 0.005–3 V respectively.

Result and discussion

As shown in Fig. 1(a), all the diffraction peaks of as-prepared PX-phase PT nanowires match well with the standard XRD pattern (JCPDS #48-0105). The PX-phase PT material has a body-centered tetragonal unit cell and contains ~5.5 Å wide pores in the *a*–*b* plane (inset in Fig. 1(a)). Fig. 1(b) presents a typical SEM images of the as-prepared PX-phase PT, showing fibrous morphology with the diameter in the range of 10 nm to more than 300 nm and the length in the range of hundreds of nanometers to over 30 μm.

The according electrochemical performance of PT as a NIB anode material with CMC and SBR as binders is evaluated by charge–discharge tests at the current intensity of 30 mA g^{-1} with the voltage ranging from 0.005 V to 3 V. As depicted in Fig. 1(c), the initial discharge/charge capacity of PT/CMC–SBR electrode is 522.3/367.6 mA h g^{-1}. An obvious gradual fading similar to those normally observed in the PX-phase PT as LIB anodes is seen in first several cycles. After 100 cycles, the capacity still remains 84.2 mA h g^{-1}. Fig. 1(d) shows the rate capability of PT/CM–SBR electrodes. The specific current is increased stepwise from 30 mA g^{-1} to 2000 mA g^{-1} every 10 cycles, and finally reverts to the initial value of 30 mA g^{-1}. It is seen that PT/CM–SBR electrode delivers discharge capacity of 263.5 mA h g^{-1} at 30 mA g^{-1} and then reduces to 166.3, 114.5 and 78.6 mA h g^{-1} at a specific current of 50, 100 and 200 mA g^{-1}, respectively. A discharge capacity of 30 mA h g^{-1} is
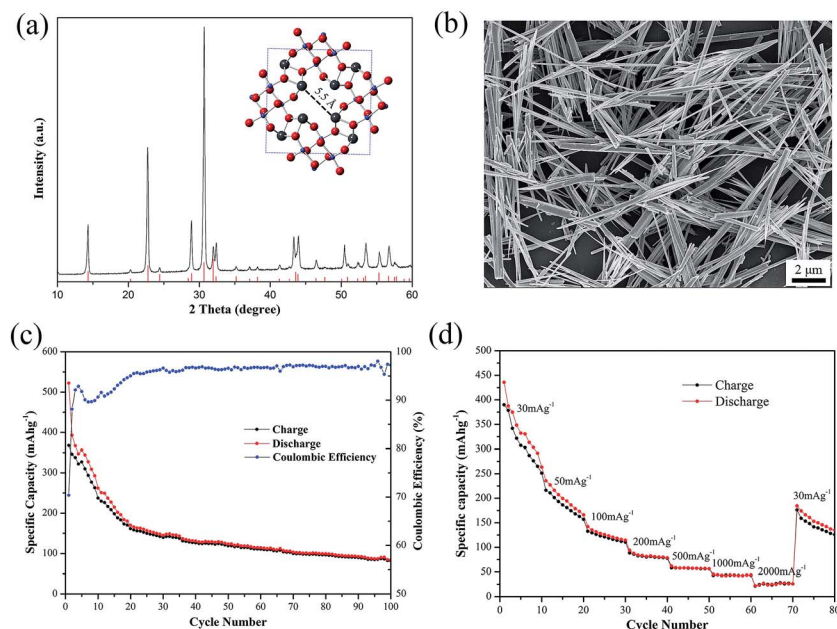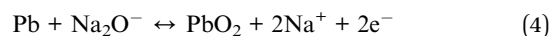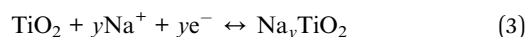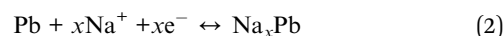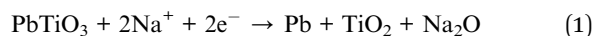
Fig. 1 (a) XRD pattern, and (b) SEM image of pristine PX-phase PT nanowires; (c) cycling capacity and coulombic efficiency of PT/CMC–SBR electrode; (d) rate capability of PT/CMC–SBR electrode. The inset in (a) shows the atomic structure of PX-phase PT within a unit cell, in which the black, blue and red balls represent Pb, Ti, O atoms, respectively.

delivered at the highest tested specific current of 2000 mA g^{-1} and 134.7 mA h g^{-1} is remained when the specific current is set back to 30 mA g^{-1}.

Cyclic voltammograms (CVs) analysis has been conducted to illuminate the Na-ions insertion/extraction mechanism of PT/CMC–SBR electrode. As presented in Fig. 2(a), the first discharge curve shows three reduction peaks, located at 0.43, 0.18 and 0.01 V respectively, whereas the peak at 0.43 V disappears in the subsequent cycles. The reduction peak at 0.43 V

corresponded to a multiphase transition $PbTiO_3 + 2Na^+ + e^- \rightarrow Pb + TiO_2 + Na_2O$. The peaks at 0.18 and 0.01 V are corresponding to the alloying process of Pb to Na$_x$Pb as well as sodium ion inserting into the super P carbon.[16,32] In the subsequent charge process, three oxidation peaks at 0.28, 0.45 and 0.58 V are corresponding to the progressive dealloying reactions from Na$_x$Pb to Pb.[32] There are two broad oxidation peaks ranging from 1.2 V to 1.5 V and two broad reduction peaks ranging from 1.4 V to 0.7 V in the CV curves, which can be attributed to the conversion reaction between Pb and PbO$_2$.[21] Based on the CV profiles and reaction mechanisms of PX-phase PT as anode materials of LIBs, the reactions that are involved in PX-phase PT anode as NIBs can be expressed as follows:

$$PbTiO_3 + 2Na^+ + 2e^- \rightarrow Pb + TiO_2 + Na_2O \tag{1}$$

$$Pb + xNa^+ + xe^- \leftrightarrow Na_xPb \tag{2}$$

$$TiO_2 + yNa^+ + ye^- \leftrightarrow Na_yTiO_2 \tag{3}$$

$$Pb + Na_2O^- \leftrightarrow PbO_2 + 2Na^+ + 2e^- \tag{4}$$

The voltage profiles (*vs.* capacity) for first three cycles are shown in Fig. 2(b). Two long potential plateaus at 0.6 V and 0.01 V and one short potential plateaus at 0.2 V appear during the initial discharge process. The potential plateaus at 0.6 V disappears in the subsequent cycles. This potential plateau corresponds to the reaction described by eqn (1), which was the main reason leading to low initial coulombic efficiency (70.38%) of PT/CMC–SBR electrode. The slope (1.2–1.8 V) that delivers a specific capacity of 100 mA h g^{-1} was corresponding
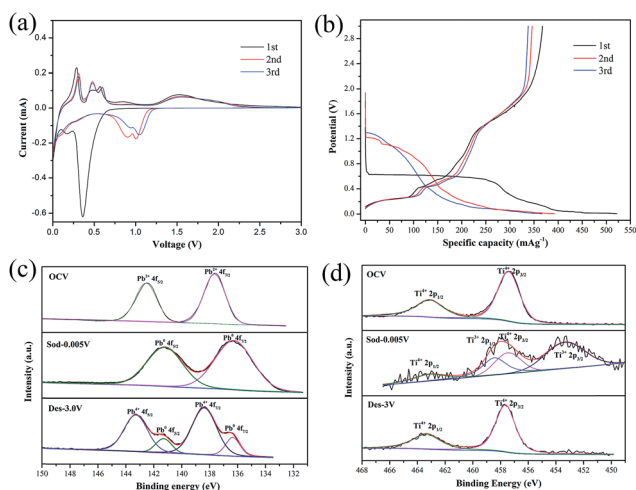

Fig. 2 (a) Cyclic voltammogram curves of PT/CMC–SBR electrode; (b) voltage profiles of selected cycles for PT/CMC–SBR electrode; XPS spectra of (c) Pb and (d) TiO$_2$ in the PT/CMC–SBR electrode at various cut-off voltages: open circuit voltage, first discharged to 0.005 V, first charged to 3.0 V.

to the reaction described by eqn (4). Different from the case for PX-phase PT LIBs, the conversion reaction between Pb and PbO_2 only proceeds in the PX-phase PT NIBs. It is first time to find this reaction in the PT/CMC–SBR electrode. Darwiche et al.[31] have suggested that the four distinct plateaus observed in the discharge process of bulk lead, corresponding to the formation of $NaPb_3$, $NaPb$, Na_9Pb_4 and $Na_{15}Pb_4$ crystalline phases sequentially, and phase transformation in the charge process is just the opposite. However, for PT/CMC–SBR electrode, the four plateaus cannot be clearly observed, especially for the second and third cycles, with only two plateaus at 1.2 and 0.01 V in the discharge process and three plateaus at 0.2, 0.4 and 0.56 V in the charge process. This indicates that the sodiation process of Pb produced by the decomposition of PX-phase $PbTiO_3$ is different from that of bulk Pb.

XPS analysis of cycled electrode is performed to further track the chemical state of Pb and Ti elements in the PT/CMC–SBR electrode (Fig. 2(c) and (d)). At open circuit voltage (OCV), the Pb 4f peaks located at 137.65 eV and 142.55 eV are consistent with the Pb^{2+} state in PX-phase $PbTiO_3$. After discharged to 0.005 V, the Pb 4f peaks shift to 136.27 eV and 141.22 eV, indicating the occurrence of reduction of Pb^{2+} to Pb^0 in the first discharge process as shown in reaction (1) and (2). Upon the completion of the subsequent charging, the peaks for Pb^{4+} (138.39 eV and 143.29 eV) appear as the dominant ones, indicating that a large portion of metallic Pb are oxidized and thus conforming the presence of reaction (4) in the PT/CMC–SBR electrode. Fig. 2(d) shows the reversible valance state change of Ti from Ti^{4+} to Ti^{3+}

in good accord with reaction (3). It is interesting to note that no appreciable reversible peaks that are expected for the insertion/de-insertion process of Na^+ in crystalline TiO_2 have been observed in the CV measurements. This is due to the amorphous nature of the formed TiO_2, similar to the case of PX-phase PT-fiber electrode in LIBs.[34]

As indicated by reaction (1), PX-phase PT has undergone a decomposition process during the first discharge. It is thus interesting to investigate their structural change induced by the reaction. Fig. 3(a) shows the microstructural image of PT/CMC–SBR electrode after first discharged to 0.005 V. It is seen that the active material has retained their integrity as wires. Nevertheless, a close inspection of the magnified TEM image (inset in Fig. 3(a)) reveals a substantial change in microstructure, leading to formation of a composite structure with 5–8 nm ultrafine nanoparticles uniformly dispersed in an amorphous matrix. The exposed crystalline fringes of the nanoparticles observed in the HRTEM images (Fig. 3(b)) as well as the SAED pattern (inset in Fig. 3(b)) indicate that those crystalline particles are *fcc* Pb nanoparticles. Fig. 3(c) shows the HRTEM image and SAED pattern of PT/CMC–SBR electrode after first charged to 3.0 V. The results show that the nanoparticles in the matrix are Pb, but their content is relatively reduced compared with Fig. 3(b). Fig. 3(d) shows the XRD of PT/CMC–SBR electrode at various cut-off voltages. Upon first discharged to 0.25 V new peaks ascribed to Pb appeared instead of PX-phase $PbTiO_3$. This change indicates the occurrence of reaction (1). The $TiO_2 \cdot Na_2O$ phase had been reported to be amorphous which explains the
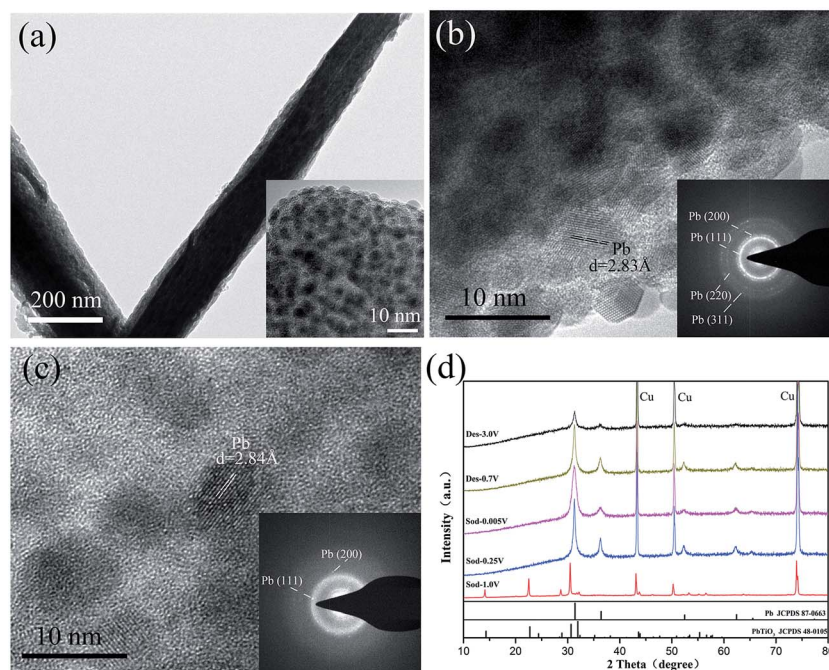

Fig. 3 (a) TEM image and (b) HRTEM image of the PT/CMC–SBR electrode first discharged to 0.005 V; (c) HRTEM image of the PT/CMC–SBR electrode first charged to 3.0 V; (d) XRD patterns of PT/CMC–SBR electrode at various cut-off voltages: first discharged to 1.0 V, first discharge to 0.25 V, first discharged to 0.005 V, first charged to 0.7 V and first charged to 3.0 V ("Cu" represents the peaks contributed from the Cu current collector substrate). The inset in (a) presents a magnified view of the wires. The inset in (b) and (c) show the corresponding selected-area electron diffraction patterns.

lack of associated Bragg peaks. The XRD of fully discharged state shows only Pb phase. While that of fully charged state also shows only Pb phase, but with much weaken intensity. And this indicates that Pb has been transformed, consisting with the result of XPS analysis.

Although the CV curves show the alloying reaction (Pb + Na$^+$ + e$^-$ $\leftrightarrow$ Na$_x$Pb) can proceed, the results of XRD and repeated TEM characterizations do not show the presence of crystalline Na$_x$Pb alloy phases. Therefore we conclude that the Na$_x$Pb alloy phases after discharge process are amorphous and alloying reaction is not fully completed. This is significantly different from the case of bulk Pb.[31] The fact that a substantial portion of metallic Pb that is reduced from pristine PT does not further participate in the sodiation reaction largely accounts for the lower capacity of PX-phase PT relative to bulk Pb. The possible reason might be ascribed to the existence of amorphous TiO$_2$·Na$_2$O matrix formed after the PT decomposition, which makes it difficult for Na$^+$ to diffuse through the amorphous surrounding to reach Pb and completely alloy with it. This is similar to the case of SnO$_2$ anode materials in NIBs.[21]

As indicated by Zhang et al.,[27] the choice of binders could have a significant influence on the anode performance in NIBs. To have a deeper view of the role of CMC/SBR binder we used, a comparative study is conducted on PX-phase PT anode with PVDF as binder. As shown in Fig. S1(a),† the specific capacity of PT/PVDF electrode is down to 26.8 mA h g^{-1} after 100 cycles, which is only one third of PT/CMC–SBR electrode (84.2 mA h g^{-1}). Fig. S1(b)† shows the rate capability of PT/PVDF electrode. The capacity of PT/PVDF electrode is dropped to 0 mA h g^{-1} when the current density is larger than 200 mA g^{-1}, while that of PT/CMC–SBR is still 100 mA h g^{-1} at 200 mA g^{-1} and 30 mA h g^{-1} at 2000 mA g^{-1}. Therefore, it is clearly seen that CMC/SBR is superior to PVDF as binder in the NIBs anode with PT nanowires as active material. To elucidate the detailed mechanism, further analysis has been performed. As shown in Fig. S1(c),† the CV curves of PT/PVDF electrode nearly coincide with that of PT/CMC–SBR electrode in the low potential range (<0.7 V). However, in the potential range higher than 0.7 V, the two broad oxidation peaks ranging from 1.2 V to 1.5 V and two broad reduction peaks ranging 1.4 V to 0.7 V in the CV curves of PT/CMC–SBR electrode are not present in PT/PVDF electrode. This pair of oxidation/reduction peaks is corresponding to the reaction described by eqn (4) and delivers a specific capacity of 100 mA h g^{-1} in the initial cycle. The missing reaction (4) in the PT/PVDF electrode is in good accord with its lower specific capacity compared to PT/CMC–SBR electrode.

SEM analysis of the cycled electrodes at different discharge/charge states is carried out to check the structural change during discharge and charge processes (Fig. 4). Upon the initial discharge, the pristine PX-phase PT wires with smooth surface (Fig. 4(a) and (e)) undertake a decomposition into Pb and TiO$_2$ and subsequent alloying process of Pb with Na, which lead to a huge volume expansion and roughened wire surface (Fig. 4(b) and (f)). In the charge process, the surface of the nanowires become smooth again accompanied with a reduction in the thickness due to deintercalation of Na ions from the matrix. However, in the case of PT/PVDF electrode, hexagonal particles appear on the surface of the electrode at 1.5 V (Fig. 4(c)), and continues growing in size and number upon further charge to 3.0 V (Fig. 4(d)) while no presence of hexagonal particles is detected in the PT/CMC–SBR electrode during the whole charge/discharge process (Fig. 4(g) and (h)). The energy dispersive analysis (EDS) result shows that the main elements in the hexagonal particles are Pb, Na and O, which excludes that the phase is PT (ESI Fig. S2†). Thus it can be inferred that instead of reaction (4) which take place within the similar potential range in the PT/CMC–SBR electrode, the Pb species have diffused out from the wires and reprecipitated as
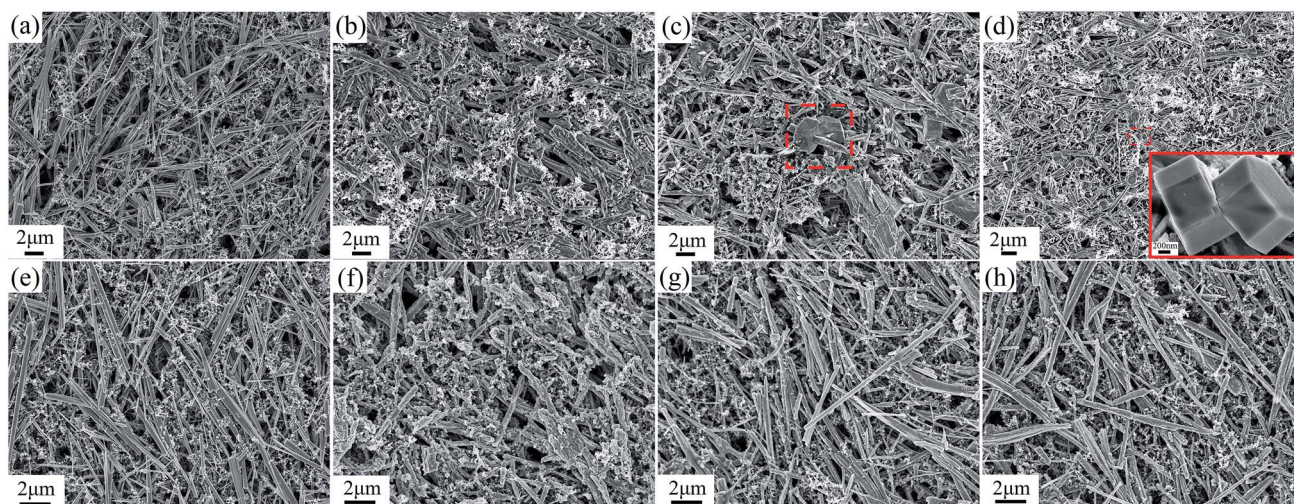

Fig. 4 (a–d) SEM images of the PT/PVDF electrodes at various cut-off voltages: (a) a pristine electrode, (b) first discharged to 0.005 V, (c) first charged to 1.5 V, (d) first charged to 3.0 V. The inset in (d) presented a magnified view of hexagonal particles. (e–h) SEM images of the PT/CMC–SBR electrodes at various cut-off voltages: (e) a pristine electrode, (f) first discharged to 0.005 V, (g) first charged to 1.5 V, (h) first charged to 3.0 V.

hexagonal particles in combination with Na and O when PVDF is employed as binder. The formed microsized hexagonal particles lead to a bigger volume change and further aggravate electrode's disintegration, resulting the inferior cyclic and rate capability of PT/PVDF electrode in NIBs.

Conclusions

In this paper, PX-phase $PbTiO_3$ nanowires is investigated as anode materials for sodium-ion batteries. PT nanowires is found to undergo an irreversible conversion reaction to transform into a composite structure composed of 5–8 nm Pb nanoparticles uniformly dispersed in the amorphous matrixes in the first discharge process. In the subsequent process, the capacity is primarily attributed to alloying reaction between Pb and Na which formed amorphous Na_xPb alloys. With different binders (CMC–SBR vs. PVDF), PT nanowires exhibit distinct electrochemical performance, PT/CMC–SBR electrode delivers a specific capacity of 84.2 mA h g^{-1} at 30 mA g^{-1} after 100 cycles, which is three times as the PT/PVDF electrode (26.8 mA h g^{-1}). The initial coulombic efficiency of PT/CMC–SBR electrode (70.38%) is also obviously higher than that of PT/PVDF (55.21%). Meanwhile, PT/CMC–SBR electrode exhibits better rate capability. It is found that compared to PT/CMC–SBR electrode, the conversion reaction between Pb and PbO_2 is missing in the PT/PVDF electrode, and that Pb active material has diffused out from the wires and reprecipitated as microsized hexagonal particles during the discharge/charge process, leading to the inferior electrochemical performance of PT/PVDF electrodes. This work manifests that binders have an important influence on the reaction mechanism between PX-phase PT and sodium ion and signifies the importance of binders to optimize the electrochemical performance for alloy anode materials in NIBs.

Acknowledgements

Notes and references

1 S. Y. Hong, Y. Kim, Y. Park, A. Choi, N. S. Choi and K. T. Lee, *Energy Environ. Sci.*, 2013, **6**, 2067–2081.

2 R. C. Massé, E. Uchaker and G. Cao, *Sci. China Mater.*, 2015, **58**, 715–766.

3 R. Berthelot, D. Carlier and C. Delmas, *Nat. Mater.*, 2011, **10**, 74–80.

4 Y. Cao, L. Xiao, W. Wang, D. Choi, Z. Nie, J. Yu, L. V. Saraf, Z. Yang and J. Liu, *Adv. Mater.*, 2011, **23**, 3155–3160.

5 E. Lee, D. E. Brown, E. E. Alp, Y. Ren, J. Lu, J. J. Woo and C. S. Johnson, *Chem. Mater.*, 2015, **27**, 6755–6764.

6 H. M. Liu, H. S. Zhou, L. P. Chen, Z. F. Tang and W. S. Yang, *J. Power Sources*, 2011, **196**, 814–819.

7 W. Tang, X. Song, Y. Du, C. Peng, M. Lin, S. Xi, B. Tian, J. Zheng, Y. Wu, F. Pan and K. P. Loh, *J. Mater. Chem. A*, 2016, **4**, 4882–4892.

8 W. Shen, H. Li, Z. Y. Guo, Z. H. Li, Q. J. Xu, H. M. Liu and Y. G. Wang, *RSC Adv.*, 2016, **6**, 71581–71588.

9 D. A. Stevens and J. R. Dahn, *J. Electrochem. Soc.*, 2001, **148**, A803–A811.

10 S. Komaba, W. Murata, T. Ishikawa, N. Yabuuchi, T. Ozeki, T. Nakayama, A. Ogata, K. Gotoh and K. Fujiwara, *Adv. Funct. Mater.*, 2011, **21**, 3859–3867.

11 M. M. Doeff, Y. P. Ma, S. J. Visco and L. C. Dejonghe, *J. Electrochem. Soc.*, 1993, **140**, L169–L170.

12 R. AlcáNtara, P. Lavela, G. F. Ortiz and J. L. Tirado, *Electrochem. Solid-State Lett.*, 2005, **8**, A222–A225.

13 L. Wu, D. Bresser, D. Buchholz, G. A. Giffin, C. R. Castro, A. Ochel and S. Passerini, *Adv. Energy Mater.*, 2015, **5**, 1401142.

14 Y. Xu, E. M. Lotfabad, H. Wang, B. Farbod, Z. Xu, A. Kohandehghan and D. Mitlin, *Chem. Commun.*, 2013, **49**, 8973–8975.

15 A. Rudola, K. Saravanan, S. Devaraj, H. Gong and P. Balaya, *Chem. Commun.*, 2013, **49**, 7451–7453.

16 A. Rudola, K. Saravanan, C. W. Mason and P. Balaya, *J. Mater. Chem. A*, 2013, **1**, 2653–2662.

17 Y. H. Xu, Y. J. Zhu, Y. H. Liu and C. S. Wang, *Adv. Energy Mater.*, 2013, **3**, 128–133.

18 N. Zhang, Y. C. Liu, Y. Y. Lu, X. P. Han, F. Y. Cheng and J. Chen, *Nano Res.*, 2015, **8**, 3384–3393.

19 S. Liao, G. Z. Yang and C. X. Wang, *RSC Adv.*, 2016, **6**, 114790–114799.

20 L. Xiao, Y. Cao, J. Xiao, W. Wang, L. Kovarik, Z. Nie and J. Liu, *Chem. Commun.*, 2012, **48**, 3321–3323.

21 J. Ding, Z. Li, H. Wang, K. Cui, A. Kohandehghan, X. Tan, D. Karpuzov and D. Mitlin, *J. Mater. Chem. A*, 2015, **3**, 7100–7111.

22 M. Gu, A. Kushima, Y. Shao, J. G. Zhang, J. Liu, N. D. Browning, J. Li and C. Wang, *Nano Lett.*, 2013, **13**, 5203–5211.

23 W. J. Zhang, *J. Power Sources*, 2011, **196**, 13–24.

24 J. Jiang, Y. Li, J. Liu, X. Huang, C. Yuan and X. W. Lou, *Adv. Mater.*, 2012, **24**, 5166–5180.

25 M. Sawicki and L. L. Shaw, *RSC Adv.*, 2015, **5**, 53129–53154.

26 Y. Yui, M. Hayashi, K. Hayashi and J. Nakamura, *Solid State Ionics*, 2016, **288**, 219–223.

27 W. J. Zhang, M. Dahbi and S. Komaba, *Curr. Opin. Chem. Eng.*, 2016, **13**, 36–44.

28 T. R. Jow, L. Y. Shacklette, M. Maxfield and D. Vernick, *J. Electrochem. Soc.*, 1987, **134**, 1730–1733.

29 S. Komaba, Y. Matsuura, T. Ishikawa, N. Yabuuchi, W. Murata and S. Kuze, *Electrochem. Commun.*, 2012, **21**, 65–68.

30 L. D. Ellis, B. N. Wilkes, T. D. Hatchard and M. N. Obrovac, *J. Electrochem. Soc.*, 2014, **161**, A416–A421.

31 A. Darwiche, R. Dugas, B. Fraisse and L. Monconduit, *J. Power Sources*, 2016, **304**, 1–8.

32 X. T. Lin, P. Li, L. Y. Shao, X. Zheng, M. Shui, N. B. Long, D. J. Wang and J. Shu, *Electrochim. Acta*, 2015, **169**, 382–394.

33 J. Wang, K. Schenk, A. Carvalho, B. Wylie-van Eerd, J. Trodahl, C. S. Sandu, M. Bonin, I. Gregora, Z. B. He, T. Yamada, H. Funakubo, P. R. Briddon and N. Setter, *Chem. Mater.*, 2011, **23**, 2529–2535.

34 Z. Shi, J. Wang, W. Wang, Y. Zhang, B. Li, Z. Lu and Y. Li, *Nano Res.*, 2015, **9**, 353–362.